# Comparison of Noise Mechanisms in High and Low Reynolds Number High-Speed Jets

J. Kastner* and M. Samimy†
*The Ohio State University, Columbus, Ohio 43235*
J. Hileman‡
*Massachusetts Institute of Technology, Cambridge, Massachusetts 02139*
and
J. B. Freund§
*University of Illinois at Urbana–Champaign, Urbana, Illinois 61801*

Direct numerical simulation results from a low Reynolds number jet and experimental results from a high Reynolds number jet were analyzed and compared to investigate the influence of the Reynolds number on the mechanisms generating jet noise. The direct numerical simulation results are for a Mach 0.9, low Reynolds number ($\mathrm{Re}_D \sim 3600$) axisymmetric jet, and the experimental results are for an ideally expanded, Mach 1.3, high Reynolds number ($\mathrm{Re}_D \sim 1.06 \times 10^6$) axisymmetric jet. Previous experimental work on the high Reynolds number jet using a three-dimensional far-field microphone array, located at 30 deg with respect to the downstream jet axis, estimated the source location and the time of generation of each large amplitude sound wave. Simultaneously with the far-field sound measurements, the source region of the flowfield was visualized using a MHz rate imaging system. In the current work, this technique is used with the direct numerical simulation data and the results are compared with the experimental data. There are many similarities between the two results including the far-field acoustic spectrum, coherence, and average waveform as well as the mean noise source location. The few differences can be attributed to the limited range of turbulence scales and the laminar initial shear layer of the low Reynolds number jet. The main conclusion is that the rapid breakdown of the large-scale structures appears to be important, perhaps the main mechanism of jet noise, independent of the Reynolds number. Right before the breakdown, the structures seem to contract in size, tilt, and eventually disintegrate. To offer a possible explanation for the observed noise mechanism, a simple one-dimensional wave packet model is shown to create more noise in the far field when truncated to simulate a breakdown.

## Nomenclature

| | | |
|---|---|---|
| $D$ | = | nozzle exit diameter |
| $f$ | = | frequency |
| $k_x$ | = | wave number in $x$-direction |
| $m$ | = | POD mode number |
| $P$ | = | acoustic pressure |
| $St_D$ | = | $fD/U_j$, Strouhal number |
| $U_c$ | = | convective velocity |
| $U_j$ | = | nozzle exit velocity (also velocity in the jet potential core) |
| $X, Y, Z$ | = | streamwise ($X$) and cross-stream ($Y$ and $Z$) coordinates (Fig. 1) |
| $\delta$ | = | percent truncation |
| $\sigma$ | = | damping coefficient |
| $\sigma_p$ | = | standard deviation of pressure |
| $\tau_c$ | = | $tU_c/D$, convective time scale |

*Graduate Student, Department of Mechanical Engineering, Gas Dynamics and Turbulence Laboratory, 2300 West Case Road. Member AIAA.

†Professor and Director, Department of Mechanical Engineering, Gas Dynamics and Turbulence Laboratory, 2300 West Case Road. Associate Fellow AIAA.

‡Post Doctoral Associate, Gas Turbine Laboratory, 77 Massachusetts Avenue. Member AIAA.

§Associate Professor, Department of Theoretical and Applied Mechanics, 104 South Wright Street. Member AIAA.

## I. Introduction

THE advent of the jet engine for aircraft immediately motivated efforts to reduce the far-field noise generated by the exhausting high-speed jet. Lighthill [1] crafted the first jet noise theory and predicted that the total radiated acoustic power would scale with the jet exit velocity to the eighth power. However, at shallow angles with respect to the jet axis, the velocity to the eighth power does not hold at all frequencies [2]. At these angles, the Strouhal numbers in the far field are similar to those of the coherent structures in the jet [3–5]. The coherent structures within turbulent shear flows were first suggested as noise sources by Mollo-Christensen [6], and the importance of these structures in entrainment and bulk mixing was further realized by Crow and Champagne [3], Brown and Roshko [7], and others.

Relations between the flowfield and the acoustic far field are often sought in the frequency domain [8]. However, such an approach will specifically miss how the dynamics of coherent structures might produce noise, so a complete understanding of the mechanisms involved requires real-time flowfield data [9]. Techniques relating measurements of the flowfield to the far field have provided insight on the potential relationship between large-scale structures and the generation of sound [5,10–14]. The flowfield data were primarily acquired as point measurements, often with intrusive probes. Because intrusive probes become sound sources when placed within the flowfield, nonintrusive planar measurements are better suited for establishing the link between the flowfield dynamics and the far-field sound.

Recently Hileman et al. [15–17] developed experimental techniques for simultaneous measurement of the far-field sound

and the flowfield. The technique involved an array of eight microphones in the far field located at 30 deg to the downstream jet axis and time resolved planar visualization of the flow. The origins of high amplitude sound waves were estimated using the microphone array whereas the flowfield evolution was imaged by a nonintrusive planar visualization technique. A proper orthogonal decomposition (POD) of flow images that were obtained during the emission of sound waves was used to reconstruct which flow features were dominant during noise generation. Rapid breakdown of the large-scale structures was observed during noise generation and this was coincident with mixed fluid reaching the jet core. These results are qualitatively similar to the instability wave breakdown described by Morrison and McLaughlin [5] in a low Reynolds number supersonic jet.

In the present work, the techniques developed and used experimentally by Hileman et al. [15–17] are implemented and used within the direct numerical simulation (DNS) of Freund [18,19]. We can thus make a direct comparison between the flow properties of the low Reynolds number jet (LReJ) and the high Reynolds number jet (HReJ). Once similarity of the mechanisms is established, we can exploit the relative strengths of computation and experiment to provide insight into the noise sources in high-speed jets and understand their Reynolds number sensitivity.

## II. Experimental and Computational Arrangements

### A. Jet Properties and Databases

Table 1 shows the flow parameters of the two jets studied. The Reynolds number was $1.06 \times 10^6$ in the experiment and is orders of magnitude larger than $3.6 \times 10^3$ in the DNS. The Mach number's influence on noise generation should be minimal because both jets have subsonic convective velocities and the Mach 1.3 jet was ideally expanded.

The near-field solution of the DNS was extended to the far field by solving the three-dimensional wave equation [18]. A detailed analysis of the computational procedure and steps taken to validate the jet against experimental results of Stromberg et al. [20] are reported in Freund [18]. This includes validation of the far-field results, which are of importance in the present study. The relation between the flow properties and the far-field radiated sound has been explored in multiple ways for the LReJ [18,21]. In the present work, the LReJ results will be analyzed using the techniques developed by Hileman et al. [15–17].

### B. Techniques

One of the enabling techniques for the simultaneous flow imaging and acoustic source localization experiments was a novel microphone array [15] that was used to estimate sources of intense sound waves (and their time evolution) reaching the far field. Another enabling technique was the MHz rate flow imaging [22]. In the present work, a virtual microphone array with similar geometry to that of the experiment has been constructed for the DNS data as shown in Fig. 1. Basically, a computational grid point in the DNS data represents a microphone in the experimental case at the same normalized location in three-dimensional space. The DNS microphone array, similar to that of the experiment, is located in the far field at 30 deg with respect to the downstream jet axis, as this is approximately the direction of most intense emission. The array is concentric with the jet and includes a total of eight microphones.

After a high amplitude noise-generating event in the jet, the sound propagates to the far field and eventually reaches the microphone array. The acoustic signals from microphones in the array are analyzed offline and times of noise generation (NG) events are
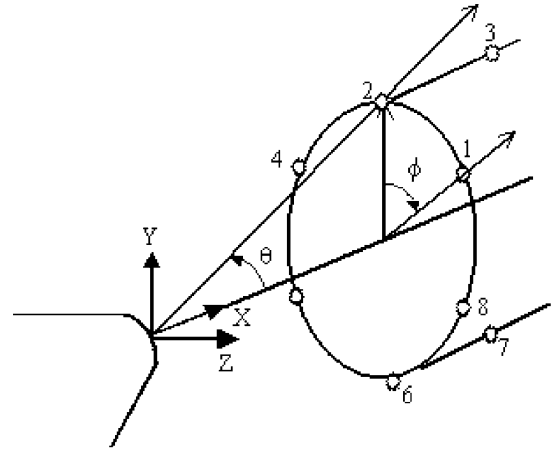


**Fig. 1 Schematic of virtual eight-microphone, three-dimensional array used in the Mach 0.9 DNS far field. Microphones 1, 2, 4, 5, 6, and 8 are at $\theta = 30$ deg and $X/D = 34$ whereas microphones 3 and 7 are at $X/D = 41$.**

determined by finding peaks in the acoustic time traces (positive or negative) that are above 1.5 times the standard deviation of the signal (Fig. 2). Increasing the number of standard deviations reduces the number of events and moves their apparent sources farther downstream [15]. Time delays estimated from the $7D$ separation in the streamwise direction between microphones 2 and 3 and microphones 6 and 7 of the inline microphones are used to find the $x$-location of the source. Time delays estimated from the 54 deg separations in the azimuthal direction for microphones 1 and 2, 2 and 4, 5 and 6, and 6 and 8 are used to locate the source in the $y$ and $z$ directions. To minimize refraction effects of sound waves passing through the shear layer of the jet, microphones closest to the noise source were used to locate the noise sources. For example, if the noise reached microphone 2 before microphone 6, then the noise most likely came from the top half of the jet and microphones 1–5 and 8 were used to locate the source. The time delay between when such a peak reaches various microphones in the array is used to determine the spatial location of noise sources within the jet through a beam-forming algorithm described by Hileman et al. [15].

In addition to locating noise sources in the jet, the post processing algorithms examined the array data for "relative quiet" (RQ) periods that *lack* far-field acoustic pressure fluctuations with amplitudes exceeding $1.5\sigma_p$ for a set length of time. Hileman et al. [16] used a minimum time duration of five convective time scales to define RQ. Because of the limited duration of the DNS data, the minimum time duration used was two convective time scales. An example of a RQ period is shown between 45 and $50\tau_c$ in Fig. 2.

Far-field acoustic data were analyzed with sound pressure levels (SPL), spatial coherence, wavelet analysis, and noise source localization. The SPL and coherence from the DNS were computed using 2048 points, sampled at 515 kHz giving a frequency resolution of 251 Hz. Correspondingly, 8192 points were used in the experiment, sampled at 200 kHz yielding a frequency resolution of 24 Hz. The DNS had only one block of data whereas the experimental data were averaged over 100 blocks.

The flowfield data of the HReJ were analyzed using image intensity due to experimental difficulties in unobtrusively obtaining temporally resolved velocity measurements. Some progress has recently been made in resolving this problem [23]. The DNS data do not have such limitations because all of the flow properties are resolved in time and space. The flowfield of the DNS is analyzed using instantaneous pressure and vorticity. After investigating the

**Table 1 Flow conditions for the two jets used in the experiment and simulation**

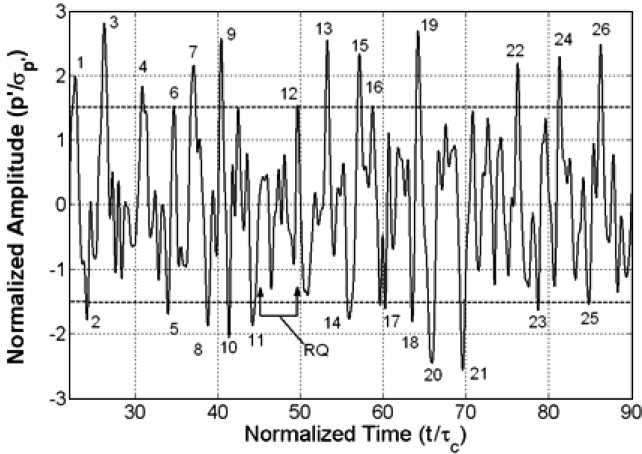|  | M | $Re_D$ | $D$, m | $U_j$, m/s | $U_c$, m/s | $P_{amb}$, atm | $f_{St_D} = 0.2$, kHz |
|---|---|---|---|---|---|---|---|
| LReJ | 0.9 | $3.6 \times 10^3$ | $7.9 \times 10^{-3}$ | 288 | 173 | 0.018 | 7.3 |
| HReJ | 1.3 | $1.06 \times 10^6$ | $25.4 \times 10^{-3}$ | 385 | 231 | 1 | 3.0 |

**Fig. 2 Acoustic pressure time trace in the far field recorded by microphone 2 for the LReJ. Peaks with amplitude greater than $1.5\sigma_p$ are identified.**



**Fig. 3 Sound pressure level spectra at $\theta = 30$ deg for the LReJ and HReJ.**

instantaneous flowfield, a POD reconstruction technique is performed to generate in an average sense the flow structure during NG and RQ periods.

The POD reconstruction technique begins with extraction of the POD modes using the snapshot method of Sirovich [24] to form an optimal basis of the pressure fluctuations within the flow. Next, the flowfield data are conditionally sampled based upon the time of NG. Then snapshots from the conditionally sampled flowfield are projected onto each POD mode to get a time coefficient. This is done for each noise event and then ensemble averaged to yield a mean time coefficient for each POD mode. Finally, the POD modes are multiplied by their corresponding mean time coefficient and the products are summed to generate a low order reconstruction of the pressure fluctuations during NG. A similar procedure is applied to snapshots before and after NG to create a phase-averaged POD reconstruction. This process was then repeated for periods of RQ. These phase-averaged reconstructions allow an investigation into the evolution of the large-scale flow structures during NG and RQ periods.

## III. Results

The far-field noise spectrum, the spatial coherence distribution in the azimuthal and streamwise directions, and the acoustic waveform for the LReJ are presented and discussed in Section III.A. Section III.B contains noise source locations and typical flowfield pressure and vorticity data during NG and RQ periods. Finally, reconstruction of the flow by using POD during NG and RQ periods are presented and discussed in Section III.C. In all steps, the LReJ and HReJ results are compared.

### A. Acoustic Far-Field Results

Figure 3 presents far-field acoustic pressure spectra at $\theta = 30$ deg for the LReJ and HReJ. Both have a broadband peak around $St_D \approx 0.2$ with amplitudes adjusted using the technique outlined by Ahuja and Bushell [2]. The more rapid high frequency spectral decay of the LReJ case is a consequence of the much lower Reynolds number.

The far-field sound spatial coherence averaged over the $St_D$ range from 0.1 to 1 in the azimuthal and streamwise directions is presented in Fig. 4 for both the LReJ and HReJ. For better spatial resolution in the DNS case, more data locations were used as shown in Fig. 1. Figure 4a shows the azimuthal coherence of the far-field sound at $\theta = 30$ deg over the azimuthal angle $f$ of 0–60 deg. The coherence levels for LReJ and HReJ are closely matched over the first 20 deg with the HReJ rolling off more quickly at larger distances. Figure 4b shows the streamwise coherence at $\theta = 30$ deg and again the coherence for the HReJ exhibits a quicker roll off. Both of these are due to the variation in Reynolds number. It was deemed important to keep the coherence level above 0.5 between adjacent microphones to
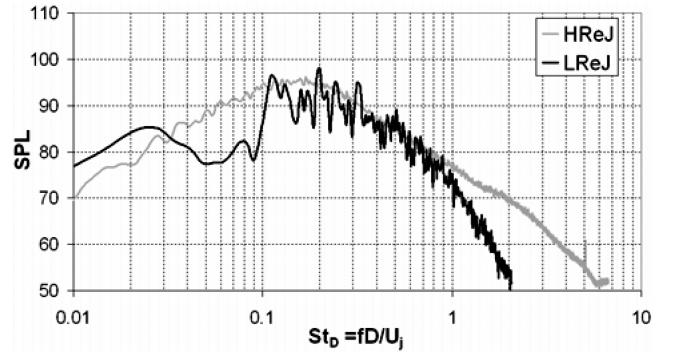
assure reliable noise source localization. For both the LReJ and HReJ, the far-field sound's azimuthal and streamwise coherence at $\theta = 30$ deg are well above 0.5, justifying the chosen microphone array geometry shown in Fig. 1.

For the $70\tau_c$ of data available in the DNS database, microphone 2 has 26 peaks that satisfy our criteria for high amplitude noise events (Fig. 2). A phase-average waveform was educed from the acoustic pressure by aligning peak event maxima (Fig. 5). The average waveform in both LReJ and HReJ resembles a Mexican-hat wavelet with the former having more oscillations away from the main peak. This is due to more periodicity of the noise-generating events, again an effect of the low Reynolds number. A Mexican-hat wavelet transformation is performed on the average waveform of both jets and the results are shown in Fig. 6. The wavelet analysis provides simultaneous information about the frequency and time of the far-field sound. Both jets have large amplitude pressure peaks that are interspersed between periods of lower sound intensity, and the majority of peak amplitudes occur near $St_D = 0.2$, consistent with acoustic spectra shown in Fig. 3.

The acoustic far fields of the two jets demonstrate many similarities. Both have large amplitude pressure peaks at a similar normalized frequency and high coherence over large azimuthal and axial distances. The differences between the spectrum, coherence, and average waveform are believed to be due to the Reynolds number disparities, in particular the smaller range in turbulence scales in the LReJ, which manifests itself most prominently in the laminar initial shear layers of lower Reynolds number jets. In the next section, the microphone array is used to estimate the source location for the high amplitude pressure peaks. Then, the pressure and vorticity fields are examined during NG and RQ periods.

### B. Flowfield Results During Noise Generation and Relative Quiet Periods

By using far-field sound pressure data and applying the beamforming algorithm, the apparent source for each of the high amplitude noise events (Fig. 2) was located within the jet. Figure 7a provides the probability distribution function of noise source location in the streamwise direction for both the LReJ and HReJ. The peak of the distribution is at a similar location of $X \sim 9.5D$ for both jets, but the distribution is more localized for the LReJ. Whereas the difference in the noise source distribution can be attributed to more coherent large-scale structures and their dynamics in the lower Reynolds number, which was also evident in the acoustic waveform (Fig. 5), the asymmetric LReJ distribution is a result of the initially laminar shear layer. The peaks are at similar downstream locations as those measured by others in high Reynolds number subsonic jets [25]. The radial distribution of noise events for the LReJ, shown in Fig. 7b, has a peak at the jet centerline, which is consistent with the HReJ results.

Because the noise source localization algorithm is in the time domain rather than the frequency domain, the array can also estimate when noise generation events occurred. The time of NG is found using the speed of sound and the distance from the array to the located noise source. The flowfield was also analyzed over a short period
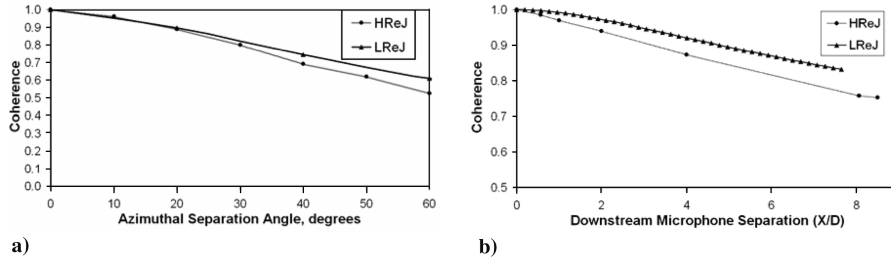
**Fig. 4 Comparison of far-field acoustic pressure average spatial coherence in the a) azimuthal and b) streamwise directions between LReJ and HReJ.**
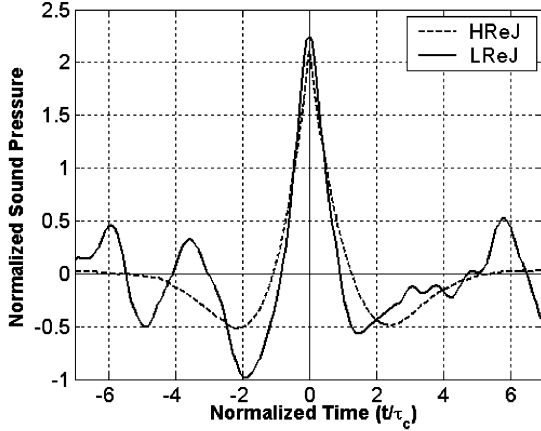


**Fig. 5 Comparison between average waveforms for LReJ and HReJ. The amplitude has been normalized by the sound pressure standard deviation.**



**Fig. 6 Comparison of wavelet transform of far-field acoustic waveform between a) LReJ and b) HReJ. The amplitude is normalized by $\sigma_p$, white is positive fluctuations, and black is negative fluctuations.**



**Fig. 7 PDF for NSL of high amplitude far-field acoustic events above $1.5\sigma$ of the acoustic pressure a) streamwise PDF for LReJ and HReJ b) radial distribution for LReJ.**

before and after the time of NG to explore the nature of the noise-producing events. For each noise event, the vorticity and pressure fields of the LReJ were investigated over a two-dimensional streamwise plane centered on $X = 9D$ and during one convective time scale.

Three typical samples of the evolution of normalized azimuthal vorticity and pressure fluctuations during noise generation process are presented in Figs. 8–10. In these figures, three snapshots of flowfield pressure (top) and corresponding vorticity (bottom) are presented before, during, and after a high amplitude noise event. The $\Delta$ symbol is at the estimated streamwise location of the noise source and the $\nabla$ symbol moves with a convective velocity of $0.6U_j$. When the two symbols line up, the high amplitude NG event noise is produced. The frames are separated by $\frac{1}{4}\tau_c$, with the estimated noise emission occurring in the middle frame. The dark and light shading are for negative and positive values, respectively.

In Fig. 8, the high amplitude noise event, event no. 3 in Fig. 2, was produced near the mean streamwise location of noise events, $X = 9.5D$. For this particular case, a structure can be identified on the upper mixing layer of the jet in both the pressure and vorticity images just before noise is produced (Fig. 8a). However, it disintegrates into smaller structures after noise production (Fig. 8c). A case where a noise event happened about a jet diameter upstream of the mean noise source location is presented in Fig. 9, event no. 5 of Fig. 2. In this case, the two sides of the shear layer begin an interaction during the high amplitude noise event. A case where a noise event happened about a jet diameter downstream of the mean noise source location is shown in Fig. 10, event no. 18 of Fig. 2. Again, the noise source seems to be where the two sides of the shear layer begin an interaction. A common feature of all three events seems to be the disintegration of a structure or structures during or right after the intense noise generation. These results agree with the experimental findings from the HReJ.

The RQ periods of course show a very different case. There are 15 periods of RQ within the low Re DNS database. Figure 11 provides three snapshots of flowfield pressure (top) and corresponding vorticity (bottom) of the jet during a period of RQ, with Fig. 11b at
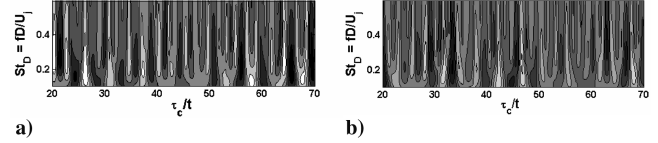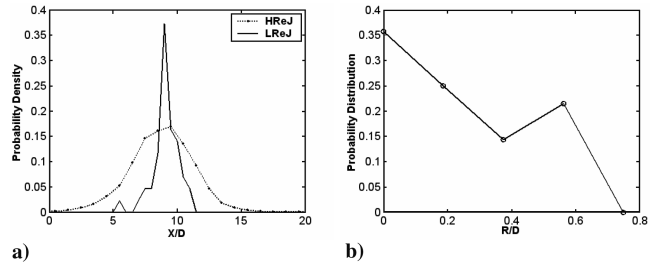
the center of the RQ period. This RQ period is labeled in Fig. 2 and occurred for $4.3\tau_c$. In the RQ case, there is no strong interaction between the top and bottom mixing layers or disintegration of any large-scale identifiable structures in any of the images.

Analyzing the evolution of single events and drawing any firm conclusion are quite subjective. To reduce the subjectivity of the interpretation, a POD reconstruction is applied to the flowfield pressure to clarify the evolution of the mixing layer during NG and RQ periods in the next section. To augment the interpretations and to support the drawn conclusions, a one-dimensional instability wave model is used.

### C. POD Reconstruction of Flowfield Pressure Fluctuations

Two-dimensional POD modes of the flowfield pressure fluctuations on the $X-Y$ plane were calculated for the LReJ. Figure 12 presents the first eight pressure POD modes, $X = 7-11D$ and $Y = \pm 1.5D$. For this window size, 29.5% of the energy is captured in the first four modes and 43.3% in the first eight modes. The instantaneous flowfield pressure was then projected onto the eight POD modes to compute the time coefficients for the mode, enabling the reconstruction of the pressure field. Figure 13 presents a POD reconstruction of the jet pressure field for the NG snapshots of Fig. 8. Comparing the NG snapshot and the POD reconstruction, the evolution of the large-scale flowfield features appears to be captured using the low order reconstruction with eight POD modes.

To further investigate the correlation between the flowfield events and the radiated high amplitude far-field sound, the phase-locked technique of Hileman et al. [16] was used. The reconstructed flowfield pressure over a time period when a high amplitude noise is produced is presented in Fig. 14. The first two images [Fig. 14a and 14b] are $\frac{1}{2}$ and $\frac{1}{4}$ a convective timescale before noise is generated, which show the presence of a large flow feature. By the time of NG
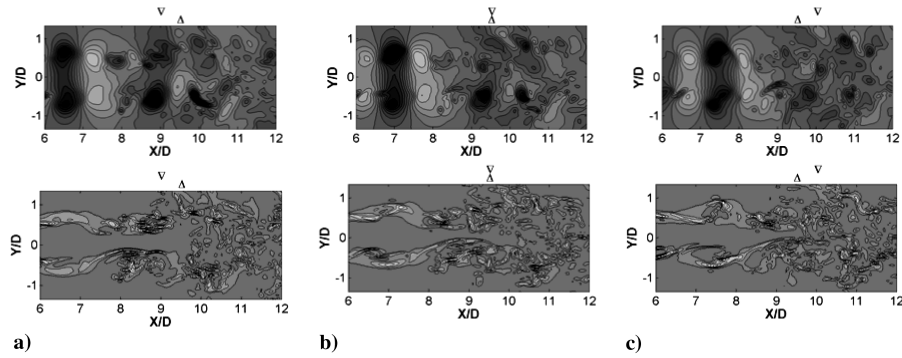
**Fig. 8    Example 1 of the evolution of jet flowfield pressure fluctuations (top) and azimuthal vorticity (bottom), $X = 6$–$12D$ and $Y = \pm 1.5D$ during NG for a strong peak ($>1.5\sigma_p$). a) $\frac{1}{4}\tau_c$ before NG, b) at time of NG, c) $\frac{1}{4}\tau_c$ after NG.**
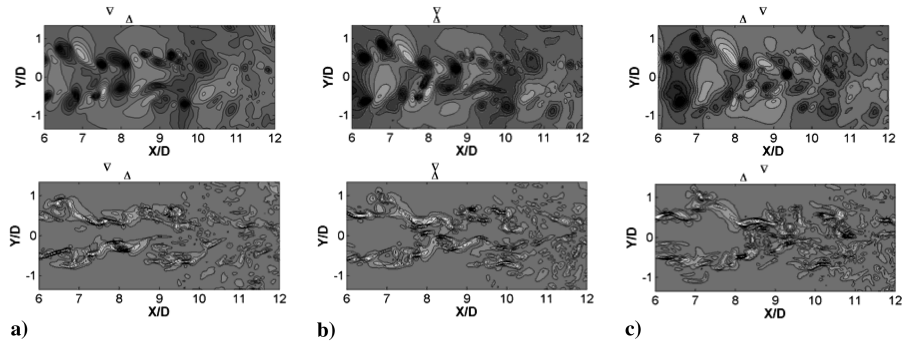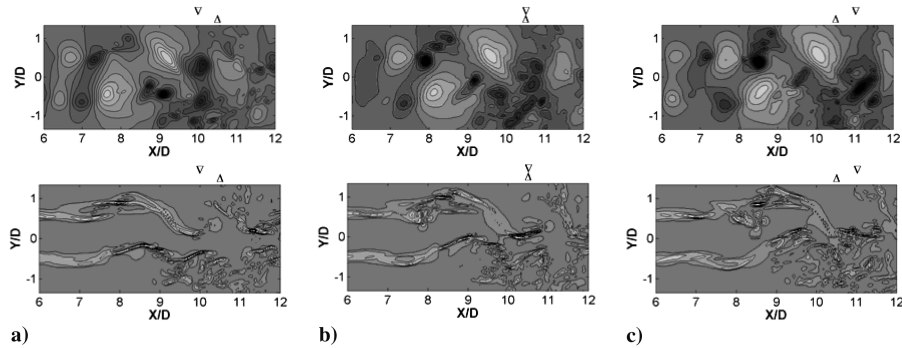


**Fig. 9    Example 2 (see the caption for Fig. 8).**

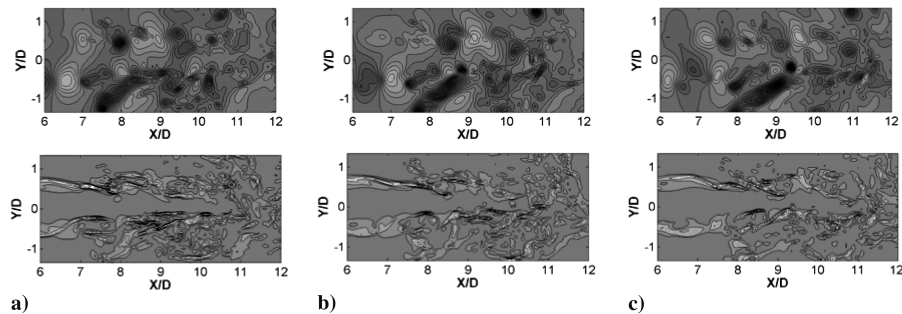

**Fig. 10    Example 3 (see the caption for Fig. 8).**



**Fig. 11    An example of the evolution of the flowfield pressure fluctuations (top) and azimuthal vorticity (bottom), $X = 6$–$12D$ and $Y = \pm 1.5D$ during a RQ period; the images are separated by $\frac{1}{4}\tau_c$ and b) is the center of the RQ period.**

(Fig. 14c) this feature has disintegrated similar to the process observed by Hileman et al. [16] in the HReJ. After noise has been produced, the jet reorganizes and large flow features reappear in the reconstructed flow (Fig. 14e). What happens before the breakdown is of importance and Fig. 15 provides a better time resolution of the flow evolution before noise generation. Before the noise-generating

event takes place, the flow features get smaller and begin to tilt toward the centerline. Again, the tilting and shrinking of structures is similar to the observations of the HReJ [16].

A similar POD reconstruction technique was performed on RQ periods (Fig. 16). There are some striking differences between the reconstructed flowfields during NG and RQ periods. The most
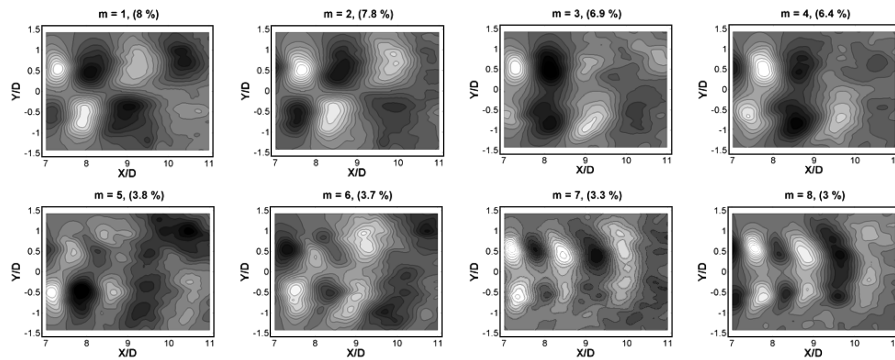
**Fig. 12    The first eight planar POD modes (on *x−y* plane) for the flowfield pressure fluctuations, *X* = 7–11*D* and *Y* = ±1.5*D*.**
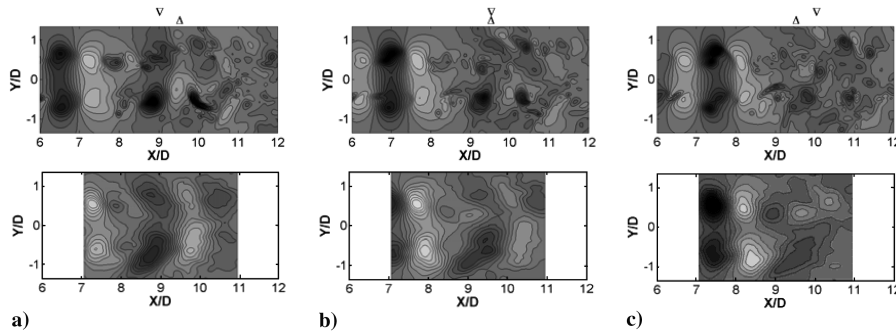


**Fig. 13    A comparison between instantaneous flowfield pressure fluctuations (top) and POD reconstruction of the flowfield pressure fluctuations (bottom) using the first eight modes. a), b), and c) are defined in Fig. 8.**
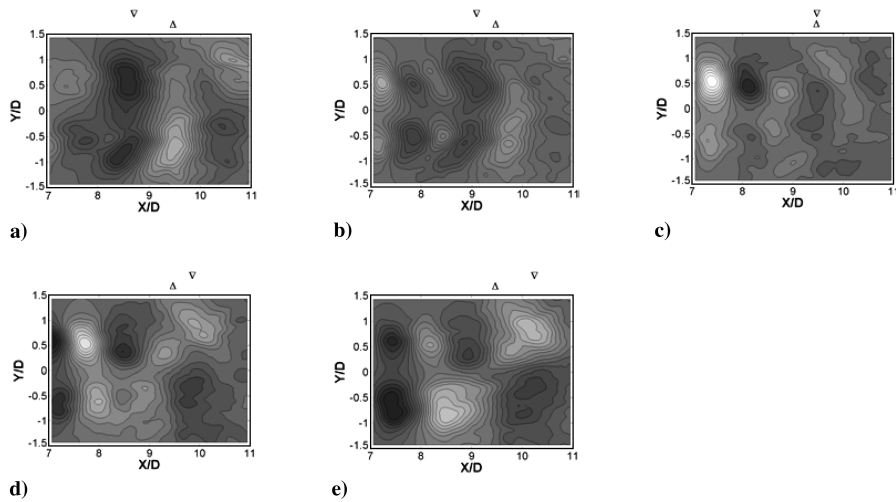


**Fig. 14    Phase-average POD reconstruction for the flowfield pressure fluctuations during the generation of high amplitude noise; a) $\frac{1}{2}\tau_c$ and b) $\frac{1}{4}\tau_c$ before NG, c) time of NG, and d) $\frac{1}{4}\tau_c$ and e) $\frac{1}{2}\tau_c$ after NG.**

notable difference is the existence of prominent flow features past 9*D* within the RQ flowfield. Within the NG flowfield, the largest flow features break down on the top of the shear layer and are not present past 9*D*. Hileman et al. [16] also observed a well-ordered flowfield during RQ periods of the HReJ. The similarities between the two jets' far-field sound and the flowfield suggest that the mechanisms making the downstream noise at high Reynolds numbers are similar to those of the low Reynolds numbers. This includes large structure breakdown as a possible noise source. This finding is also consistent with the instability wave breakdown observed by Morrison and McLaughlin [5] in their low Reynolds number supersonic jet.

Truncation of a simple one-dimensional wave packet can be used to model the breakdown of flow structures in a simplistic fashion. Similar modeling techniques have been used in previous jet noise studies [26]. A one-dimensional wave packet without breakdown is

given by Eq. (1) and is shown in Fig. 17a

$$S(x) = e^{-\sigma x^2} e^{ik_x x} \{1 + \delta[\tan(\zeta x) + 1]/2\} \qquad (1)$$

where $\sigma = 0.3$, $k_x = 2p$, and $\delta = 0$. The wave packet is symmetric about the peak amplitude. To model the breakdown, the wave packet is truncated by a window function (by setting $\delta > 0$) and the symmetry is broken beyond its maximum (Fig. 17a). These two wave packets are then extended to the far field by

$$P(x_f, y_f) = -\frac{1}{4\pi} \int_{-\infty}^{+\infty} \frac{S(x) e^{i\omega \sqrt{(x_f-x)^2 + y_f^2}}}{\sqrt{(x_f - x)^2 + y_f^2}} \, dx \qquad (2)$$

Figure 17b shows the intensity of the far-field sound in the cylindrical
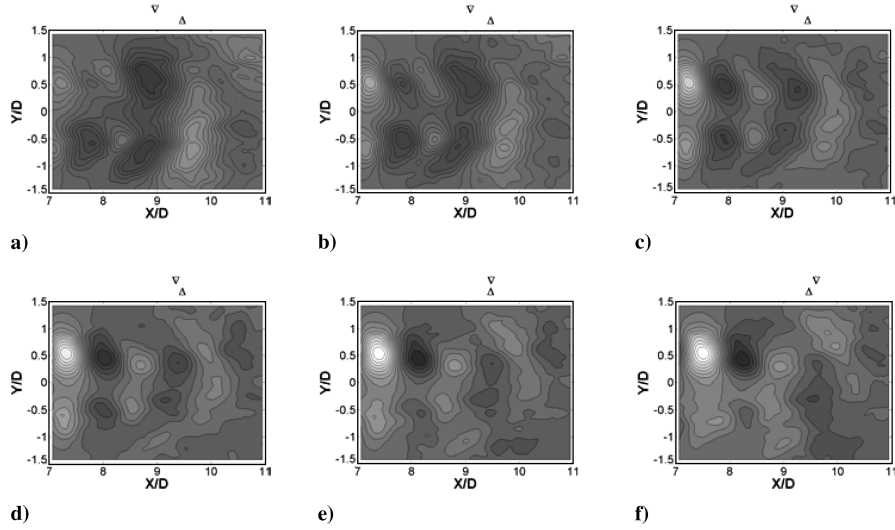
**Fig. 15   Phase-average POD reconstruction for the flowfield pressure fluctuations during high amplitude noise generation; a) $5/16\tau_c$ before NG to d) $1/16\tau_c$ before NG, e) time of NG, and f) $1/16\tau_c$ after NG.**
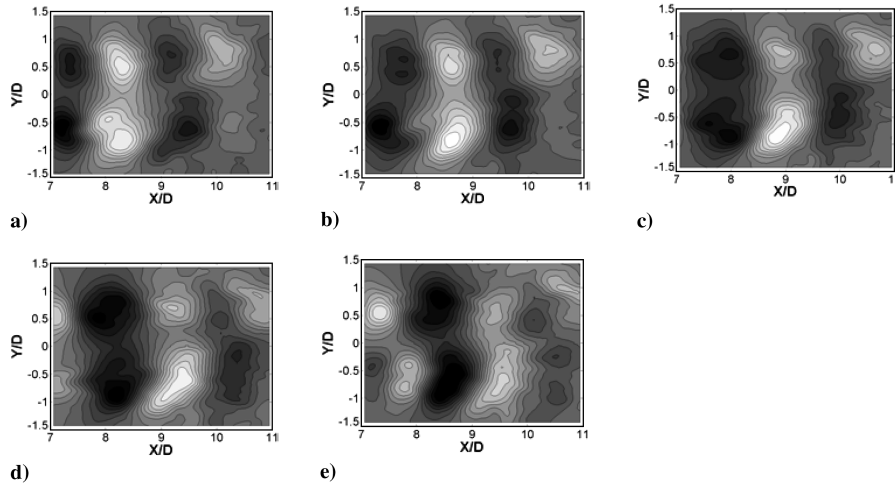


**Fig. 16   Phase-average POD reconstruction of the flowfield pressure fluctuations, $X = 7$–$11D$ and $Y = \pm 1.5D$ for periods of RQ over one convective time scale equally spaced from a) to e).**
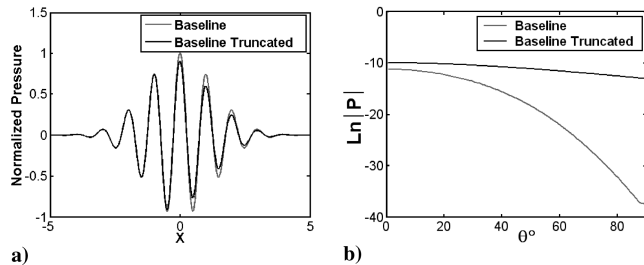


**Fig. 17   A wave packet simulating a) jet noise source (baseline) and with truncation (simulating structures breakdown) and b) far-field radiated noise for the two packets.**

coordinates $(r_f, \theta_f)$ for both the baseline and truncated sources. The result shows that far-field radiation from the truncated wave packet, modeling the breakdown, has much higher intensity (Fig. 17b).

## IV.   Summary

Previously, a far-field azimuthal array of eight microphones and simultaneous acquisition of planar flow images had been used in a high Reynolds number, ideally expanded Mach 1.3 jet (HReJ) to investigate noise sources that radiate at shallow angles with respect to

the jet axis (i.e., the approximate direction of peak radiation). This array and its associated beam-forming algorithm have the capability of estimating the time and location where large amplitude noise events are produced. A similar technique was applied to DNS data of a low Reynolds number, Mach 0.9 jet (LReJ). The results were presented, discussed, and compared with those of the experimental results from the HReJ.

The results showed that the LReJ and HReJ have many similarities in the acoustic field and mixing layer development during noise generation. Far-field acoustic spectra from both jets have a broadband peak around $St_D$ of 0.2 and the azimuthal and streamwise coherence show similar behavior at $\theta = 30$ deg. For both jets, the average far-field acoustic waveform is similar to the Mexican-hat wavelet, and a Mexican-hat wavelet transformation demonstrates a similar distribution of energy. Regardless of Reynolds number, the noise source distribution peaks on the jet centerline near $X = 9.5D$.

Two characteristic phenomena dominate the instantaneous jet pressure and vorticity field during noise generation. The first is an interaction between the two sides of the shear layer, and the second is the breakdown of prominent large-scale structures. A phase-averaged POD reconstruction referenced to the moment of noise generation suggests that the rapid breakdown of the large-scale structure is a possible mechanism of jet noise for the LReJ. Right before the breakdown, the structures tilt and the two sides of the mixing layer interact. During RQ periods, such breakdowns were not

observed. These results are consistent with the experimental observations of the HReJ.

A simple one-dimensional wave packet was used as a source model. Truncation of this wave packet was used to model the breakdown of flow structures in a simplistic fashion. The results showed that far-field radiation from the truncated wave packet had much higher intensity, which seems to be the main noise-generating mechanism in jets.

## Acknowledgments

## References

[1] Lighthill, M. J., "On Sound Generated Aerodynamically, Part 1: General Theory," *Proceedings of the Royal Society of London A*, Vol. 211, 1952, pp 564–586.

[2] Ahuja, K. K., and Bushell, K. W., "An Experimental Study of Subsonic Jet Noise and Comparison with Theory," *Journal of Sound and Vibration*, Vol. 30, No. 3, 1973, pp. 317–341.

[3] Crow, S. C., and Champagne, F. H., "Orderly Structure in Jet Turbulence," *Journal of Fluid Mechanics*, Vol. 48, 1971, pp. 547–591.

[4] Fisher, M. J., Harper-Bourne, M., and Glegg, S. A. L., "Jet Engine Source Location: The Polar Correlation Technique," *Journal of Sound and Vibration*, Vol. 51, No. 1, 1977, pp. 23–54.

[5] Morrison, G. L., and McLaughlin, D. K., "Noise Generation by Instabilities in Low Reynolds Number Supersonic Jets," *Journal of Sound and Vibration*, Vol. 65, No. 2, 1979, pp. 177–191.

[6] Mollo-Christensen, E., "Jet Noise and Shear Flow Instability Seen from an Experimenter's Viewpoint," *Journal of Applied Mechanics*, Vol. 89, No. 1, 1967, pp. 1–7.

[7] Brown, G. L., and Roshko, A., "On Density Effects and Large Structure in Turbulent Mixing Layers," *Journal of Fluid Mechanics*, Vol. 64, 1974, pp. 715–816.

[8] Fuchs, H. V., "On the Application of Mirror, Telescope, and Polar Correlation Techniques to Jet Noise Source Location," *Journal of Sound and Vibration*, Vol. 58, No. 1, 1978, pp. 117–126.

[9] Crighton, D. G., "Basic Principles of Aerodynamic Noise Generation," *Progress in Aerospace Sciences*, Vol. 16, No. 1, 1975, pp. 31–96.

[10] Lee, H. K., and Ribner, H. S., "Direct Correlation of Noise and Flow of a Jet," *Journal of the Acoustical Society of America*, Vol. 52, 1972, pp. 1280–1290.

[11] Siddon, J. E., "On Noise Mechanisms. Noise Source Diagnostics Using Causality Correlation," AGARD CP, Vol. 131, 1973.

[12] Sarohia, V., and Massier, P. F., "Experimental Results of Large-Scale Structures in Jet Flows and their Relation to Jet Noise Production," AIAA Paper 77-1350, 1977.

[13] Schaffar, M., "Direct Measurements of the Correlation Between Axial In-Jet Velocity Fluctuations and Far Field Noise near the Axis of a Cold Jet," *Journal of Sound and Vibration*, Vol. 64, 1979, pp. 73–83.

[14] Panda, J., and Seasholtz, R. G., "Experimental Investigation of Density Fluctuations in High-Speed Jets and Correlation with Generated Noise," *Journal of Fluid Mechanics*, Vol. 450, 2002, pp. 97–130.

[15] Hileman, J., Thurow, B., and Samimy, M., "Development and Evaluation of a 3-D Microphone Array to Locate Individual Acoustic Sources in a High-Speed Jet," *Journal of Sound and Vibration*, Vol. 276, 2004, pp. 649–669.

[16] Hileman, J., Caraballo, E., Thurow, B., and Samimy, M., "Large-Scale Structure Evolution and Sound Emission in High-Speed Jets: Real-Time Visualization with Simultaneous Acoustic Measurements," *Journal of Fluid Mechanics*, Vol. 544, 2005, pp. 277–307.

[17] Hileman, J., Thurow, B., and Samimy, M., "Exploring Noise Sources Using Simultaneous Acoustic Measurements and Real-Time Flow Visualization in Jets," *AIAA Journal*, Vol. 40, No. 12, 2002, pp. 2382–2392.

[18] Freund, J. B., "Noise Sources in a Low-Reynolds-Number Turbulent Jet at Mach 0.9," *Journal of Fluid Mechanics*, Vol. 438, 2001, pp. 277–305.

[19] Freund, J. B., "Noise-Source Turbulence Statistics and the Noise from a Mach 0.9 Jet," *Physics of Fluids*, Vol. 15, No. 6, 2003, pp. 1788–1799.

[20] Stromberg, J. L., McLaughlin, D. K., and Troutt, T. R., "Flow Field and Acoustic Properties of a Mach Number 0.9 Jet at a Low Reynolds Number," *Journal of Sound and Vibration*, Vol. 72, No. 2, 1980, pp. 159–176.

[21] Freund, J. B., and Colonius, T., "POD Analysis of Sound Generation by a Turbulent Jet," AIAA Paper 2002-0072, 2002.

[22] Thurow, B., Hileman, J., Lempert, W., and Samimy, M., "A Technique for Real-Time Visualization of Flow Structure in High-Speed Flows," *Physics of Fluids*, Vol. 14, No. 10, 2002, pp. 3449–3452.

[23] Thurow, B., Jiang, N., Lempert, W., and Samimy, M. "Development of Megahertz-Rate Planar Doppler Velocimetry for High-Speed Flows," *AIAA Journal*, Vol. 43, No. 3, 2005, pp. 500–511.

[24] Sirovich, L., "Turbulence and the Dynamics of Coherent Structures, Part 1: Coherent Structures," *Quarterly of Applied Mathematics*, Vol. 45, No. 3, 1987, pp. 561–571.

[25] Venkatesh, S. R., Polak, D., and Narayanan, S., "Beamforming Algorithm for Distributed Noise Source Localization and Its Application to Jet Noise," *AIAA Journal*, Vol. 41, No. 7, 1994, pp. 1238–1246.

[26] Ffowcs-Williams, J. E., and Kempton, A. J., "The Noise from the Large-Scale Structure of a Jet," *Journal of Fluid Mechanics*, Vol. 84, Pt. 4, 1978, pp. 673–694.